Transferable screened range-separated hybrid functionals for electronic and optical properties of van der Waals materials

María Camarasa-Gómez ⬤,[1] Ashwin Ramasubramaniam ⬤,[2,3] Jeffrey B. Neaton,[4,5,6] and Leeor Kronik ⬤[1]

[1]*Department of Molecular Chemistry and Materials Science, Weizmann Institute of Science, Rehovoth 7610001, Israel*
[2]*Department of Mechanical and Industrial Engineering, University of Massachusetts Amherst, Amherst, Massachusetts 01003, USA*
[3]*Materials Science and Engineering Graduate Program, University of Massachusetts Amherst, Amherst, Massachusetts 01003, USA*
[4]*Department of Physics, University of California, Berkeley, California 94720, USA*
[5]*Materials Sciences Division, Lawrence Berkeley National Laboratory, Berkeley, California 94720, USA*
[6]*Kavli Energy NanoSciences Institute at Berkeley, University of California, Berkeley, California 94720, USA*

The accurate description of electronic properties and optical absorption spectra is a long-standing challenge for density functional theory. Recently, the introduction of screened range-separated hybrid (SRSH) functionals for solid-state materials has allowed for the calculation of fundamental band gaps and optical absorption spectra that are in very good agreement with many-body perturbation theory. However, since solid-state SRSH functionals are typically tuned to reproduce the properties of bulk phases, their transferability to low-dimensional structures, which experience substantially different screening than in the bulk, remains an open question. In this work, we explore the transferability of SRSH functionals to several prototypical van der Waals materials, including transition-metal sulfides and selenides, indium selenide, black phosphorus, and hexagonal boron nitride. Considering the bulk and a monolayer of these materials as limiting cases, we show that the parameters of the SRSH functional can be determined systematically, using only the band-edge quasiparticle energies of these extremal structural phases as fitting targets. The resulting SRSH functionals can describe both electronic band structures and optical absorption spectra with accuracy comparable to more demanding *ab initio* many-body perturbation theory (GW and Bethe-Salpeter equation) approaches. Selected examples also demonstrate that the SRSH parameters, obtained from the bulk and monolayer reference structures, display good accuracy for band structures and optical spectra of bilayers, indicating a degree of transferability that is independent of the fitting procedure.

I. INTRODUCTION

van der Waals (vdW) layered materials have been in the spotlight for almost two decades [1–3], attracting an enormous amount of attention since the experimental isolation of graphene in 2004 [4,5]. These materials present an inherently wide range of structural, electronic, and optical properties, which is vastly enhanced by the possibility of combining layers (e.g., through heterostructuring, as well as relative twisting or sliding) to allow for additional tuning of their physicochemical properties [1–3,6–12].

As the space of vdW materials and their derivatives continues to expand, there is an ever growing need for a reliable theoretical description of their electronic and optical properties, particularly band structures and optical absorption spectra. Presently, state-of-the-art first-principles calculations of these properties in crystalline materials are based mostly on *ab initio* many-body perturbation theory (MBPT) [13,14]. *Ab initio* MBPT is usually employed in practice by using the GW approximation [15] with input from a (generalized) Kohn-Sham eigensystem to obtain single quasiparticle excitation energies and the Bethe-Salpeter equation (BSE) [16,17] to calculate neutral excitation energies and optical absorption spectra. Indeed, GW-BSE has been found to be very successful in the interpretation and even prediction of electronic and optical properties in vdW materials (e.g., Refs. [18–23]). However, GW-BSE calculations are relatively expensive computationally [24–26]. GW-BSE calculations can become prohibitively expensive especially when supercells are called for, e.g., in the calculation of defects or of twisted multilayer structures. Therefore, there remains a need for alternative computational approaches that can provide results with similar accuracy at a substantially lower computational cost.

A first-principles alternative to MBPT is density functional theory (DFT) [27,28], as well as its extension to excited states, namely time-dependent DFT (TDDFT) [29,30]. However, it is well known that (TD)DFT with common approximate functionals often fails in the prediction of electronic and optical excitations in solids [14]. One promising recent approach within DFT is that of the tuned screened range-separated hybrid functional (SRSH) [31,32]. This is important, because although the formal scaling of GW and of DFT with a hybrid functional is the same, in practice the latter can be markedly faster and require substantially less memory [33,34], primarily owing to the lack of explicit construction of the dielectric matrix.

Originally applied primarily to molecular solids [31,35–37], tuned SRSH functionals have recently been found to be extremely useful in the determination of fundamental gaps and optical spectra of semiconductors and insulators [38–49]. Moreover, recently a nonempirical optimally tuned SRSH approach that is applicable to a general semiconductor or insulator has been found to be quantitatively predictive for a wide range of materials, from narrow-gap semiconductors to wide-gap insulators [41,42,50].

A key feature of SRSH functionals is the proper incorporation of dielectric screening in the long-range exchange, which assures the correct asymptotic decay of the Coulomb tail [31,32,35,51,52]. However, in vdW materials the dielectric constant varies with the number of layers between its bulk value and unity—formally, the correct asymptotic limit for screening in a monolayer [53,54]—introducing a potentially large structure dependence to the parameters of the SRSH functional. Therefore, an open question remains as to whether an SRSH functional that is optimally tuned, say, for the bulk phase of a material, would be transferable to lower-dimensional structures.

In this article, we expand our prior work [39] on assessing and addressing this topic to encompass a broad range of semiconducting and insulating vdW materials, exploring both monolayers (2D materials) and bulk phases of Mo- and W-based transition-metal dichalcogenides, indium selenide, black phosphorus, and hBN, as well as bilayers of MoS_2 and hBN. We find that SRSH functionals can be tuned, using only a single quasiparticle energy gap at the band edges of the 2D and bulk phases, to produce band structures that are in excellent agreement with GW calculations over the entire Brillouin zone. Furthermore, we demonstrate that time-dependent (TD) SRSH calculations can produce optical absorption spectra for vdW semiconductors that are in very good agreement with spectra from GW-BSE calculations without any input from the latter in the tuning procedure, rendering the TD-SRSH approach truly predictive. We also explore the transferability of the SRSH parameters—derived for 2D and bulk phases—to bilayers of MoS_2 and h-BN and show that their band structures continue to be in good agreement with GW calculations.

II. THEORY OF THE SRSH FUNCTIONAL

In the SRSH approach, the Coulomb operator is partitioned into short range (SR) and long range (LR) components through the introduction of three parameters, α, β, γ, as follows [51,52]:

$$\frac{1}{r} = \frac{\alpha + \beta\,\mathrm{erf}(\gamma r)}{r} + \frac{1 - [\alpha + \beta\,\mathrm{erf}(\gamma r)]}{r}, \qquad (1)$$

where $\mathrm{erf}(\cdot)$ is the error function, r is the interelectron distance, and γ is a range-separation parameter. The first term of Eq. (1) is treated using exact exchange while the second term is treated using a semilocal approximation. The parameter α therefore sets the fraction of exact exchange in the short range, the sum of parameters $\alpha + \beta$ sets the fraction of exact exchange in the long range, and $1/\gamma$ provides a length scale for the crossover from short- to long-range behavior, interpolated smoothly by the error function [55]. To enforce a correct asymptotic behavior of the screened Coulomb operator via

appropriate dielectric screening, we impose the condition $\alpha + \beta = 1/\epsilon_\infty$, where ϵ_∞ is the high-frequency scalar (orientationally averaged) dielectric constant [35]. Enforcing this limit is essential to capturing excitonic effects in solid-state systems [35,38,56]. The above relation fixes the value of β, given a choice of α, in terms of ϵ_∞, leaving two free parameters: α and γ. This approach neglects anisotropy and approximates the dielectric constant as a scalar, i.e., $\epsilon_\infty = \mathrm{Tr}[\boldsymbol{\epsilon}_\infty]/3$. For 2D systems, we set $\epsilon_\infty = 1$, which is the correct asymptotic limit of screening in the long range for an isolated 2D system [53,54].

With these ingredients at hand, the exchange potential of the SRSH functional, derived within generalized Kohn-Sham theory [57–60], is represented by the nonmultiplicative potential operator

$$v_x^{\mathrm{SRSH}} = \alpha v_{\mathrm{XX}}^{\mathrm{SR}} + (1 - \alpha)v_{\mathrm{SL}}^{\mathrm{SR}} + \frac{1}{\epsilon_\infty}v_{\mathrm{XX}}^{\mathrm{LR}} + \left(1 - \frac{1}{\epsilon_\infty}\right)v_{\mathrm{SL}}^{\mathrm{LR}},$$
$$(2)$$

where the subscripts "x," "XX," and "SL" denote exchange, exact (Fock) exchange, and semilocal exchange, respectively.

In this work, we follow the approach of Ref. [39] to obtain the parameters α, γ, and ϵ_∞ that fully determine the SRSH functional for a given material. First, the scalar dielectric constant, ϵ_∞, for bulk phases is determined nonempirically using the random phase approximation [61] (RPA) that includes local-field effects at the Hartree level of a (semi)local functional. Other approaches are equally valid, but we choose to use the RPA to maintain consistency between the treatment of the dielectric response in the DFT and the GW calculations. The calculated values of ϵ_∞ for the bulk phases of various materials studied here are listed in Table I. For monolayers and bilayers, we use a value of $\epsilon_\infty = 1$, as discussed above. To determine suitable values of α and γ for each material, we perform GW calculations to determine the quasiparticle gaps for the bulk and monolayer structures. For monolayers, these quasiparticle gaps are extrapolated to the limit of infinite vacuum. Further details can be found in Secs. S1 and S2 of the Supplemental Material (SM) [62]. We then perform a sweep over the $\alpha - \gamma$ parameter space and calculate the corresponding SRSH band gaps for pairs of values (α, γ). We quantify the error in the SRSH calculation, relative to the reference GW result, by the difference between the quasiparticle and SRSH band gaps at a particular k point, $\Delta E_g = E_g^{\mathrm{GW}} - E_g^{\mathrm{SRSH}}$. We find that it is generally sufficient to ensure that $\Delta E_g = 0$ at just one high-symmetry k point, which we pick to correspond to the smallest direct band gap.

As noted in prior work [38–40,63], the choice of α and γ is not unique for a particular material (or phase) and the tuning procedure outlined above generally leads to a continuum of values that lie on a "zero-crossing" line, $\Delta E_g = 0$, of the $\Delta E_g(\alpha, \gamma)$ surface. Given two phases—the bulk and monolayer—the intersection of their individual zero-crossing lines leads to a unique set of parameters, (α^*, γ^*), that is simultaneously optimal for both phases. It is this optimal pair that is finally used for computing electronic and optical properties of the various materials.

Using this procedure we determine transferable pairs, (α^*, γ^*), for various vdW materials and compare their electronic band structures against those obtained from GW

TABLE I. Brillouin zone sampling, tuned SRSH parameters (α^*, γ^*), average inverse macroscopic dielectric constant (ϵ_∞^{-1}), GW band gap (E^{GW}), GW-BSE optical gap ($E_{opt}^{GW\text{-}BSE}$), SRSH band gap (E^{SRSH}, fitted to an extrapolated GW quasiparticle band gap), and TD-SRSH optical gap ($E_{opt}^{TD\text{-}SRSH}$), for the various materials studied in this article. Additional computational details are given in Secs. S1-S3 of the SM. Band gaps and optical gaps are calculated at the K point for the TMDC materials (WS$_2$, WSe$_2$, MoSe$_2$) and at the Γ point for black phosphorus (BP) and InSe.

Material	Phase	**k** grid	α^*	γ^* (Å^{-1})	ϵ_∞^{-1}	E^{GW} (eV)	$E_{opt}^{GW\text{-}BSE}$ (eV)	E^{SRSH} (eV)	$E_{opt}^{TD\text{-}SRSH}$ (eV)
WS$_2$	Bulk	$12 \times 12 \times 4$	0.102	0.019	0.093	2.32	2.22	2.29	2.21
	1L	$18 \times 18 \times 1$			1.0	2.70	2.29	2.66	2.32
WSe$_2$	Bulk	$12 \times 12 \times 4$	0.094	0.015	0.084	1.97	1.91	1.94	1.89
	1L	$18 \times 18 \times 1$			1.0	2.34	1.98	2.28	1.99
MoSe$_2$	Bulk	$12 \times 12 \times 4$	0.083	0.015	0.079	1.76	1.70	1.74	1.74
	1L	$18 \times 18 \times 1$			1.0	2.06	1.72	2.04	1.78
BP	Bulk	$8 \times 8 \times 4$	0.170	0.035	0.095	0.49	0.40	0.56	0.32
	1L	$15 \times 15 \times 1$			1.0	1.89	1.37	1.95	1.38
InSe	Bulk	$9 \times 9 \times 4$	0.149	0.021	0.121	1.15	1.05	1.21	1.10
	1L	$15 \times 15 \times 1$			1.0	2.90	2.67	2.87	2.76

calculations. We also report optical absorption spectra obtained from linear response [64] TD-SRSH calculations [31,37,38] and compare the results against GW-BSE calculations within the Tamm-Dancoff approximation [65].

III. RESULTS AND DISCUSSION

In this section, we apply the methodology described in Sec. II to representative vdW materials: these include the transition-metal dichalcogenides (TMDCs) WS$_2$, WSe$_2$, and MoSe$_2$, black phosphorus (BP), and InSe. These materials range from medium- to small-gap semiconductors.

A. Transition-metal dichalcogenides: WS$_2$, WSe$_2$, and MoSe$_2$

WS$_2$, WSe$_2$, and MoSe$_2$ are semiconductors that crystallize in the trigonal prismatic 2H phase (space group $P\bar{3}m1$) in their ground state. Figures 1(a)–1(c) display contour plots of the error in the band gap, ΔE_g, as a function of the SRSH parameters for bulk and monolayers of the three materials. Interestingly, the errors in the band gap present similar trends across this group of materials: the bulk phases exhibit a very small degree of acceptable variation in the fraction of short-range exact exchange, α, whereas this parameter can vary more widely for monolayers. It is also clear from these figures that optimizing the SRSH for just one phase can lead to rather large errors for the other phase. For example, selecting acceptable values of (α, γ) for bulk WS$_2$ at the extremes of the $\alpha - \gamma$ plot [Fig. 1(a)] leads to large errors in the predicted band gap of the monolayer, ranging from -0.122 eV for (α, γ) = (0.102, 0.010 Å^{-1}) to 2.33 eV for (α, γ) = (0.116, 0.248 Å^{-1}). Conversely, optimizing the SRSH purely for monolayer WS$_2$ results in errors in the bulk band gap ranging from 0.030 eV for (α, γ) = (0.011, 0.044 Å^{-1}) to 0.049 eV for (α, γ) = (0.113, 0.010 Å^{-1}). The point of intersection of the zero crossings of the gap deviation surfaces (α^*, γ^*) = (0.102, 0.019 Å^{-1}) simultaneously renders the error in the band gap zero for both phases. Similar behavior is observed for WSe$_2$ and MoSe$_2$.

Table I displays the optimal parameters, α^* and γ^*, along with the RPA dielectric constants, ϵ_∞, as well computed GW,

GW-BSE, SRSH, and TD-SRSH results. Our GW and GW-BSE results are in good agreement with past literature—see Tables I and II in Sec. S4 of the SM for a detailed comparison. Figure 1 displays the corresponding SRSH band structures along with the corresponding GW band structures. As the SRSH functionals were tuned to reproduce GW band gaps extrapolated to infinite interlayer separation and infinite k-point sampling (see Sec. S2 of the SM), the outcome of a particular unextrapolated GW calculation will always differ to some extent from the SRSH result. For example, for WS$_2$, the unextrapolated GW band gap for the monolayer (at the K point) is 40 meV larger than the SRSH band gap and the unextrapolated GW band gap for the bulk (at the K point) is 30 meV larger than its SRSH counterpart. Similar differences ($\sim$20 meV) are found for MoSe$_2$ and WSe$_2$. The above small differences notwithstanding, Figs. 1(d)–1(i) show very good agreement between the GW and SRSH band structures for all three, especially at the band edges. Qualitatively, the deviations are somewhat larger for the bulk than for the monolayers, particularly for the selenides. These deviations also become more apparent deeper into the valence or conduction band, which is generally expected when using SRSH eigenvalues as approximate quasiparticle excitation energies [58,66,67]. These deeper bands, however, are less relevant to electronics applications or to the low-energy optical absorption spectrum. The mean absolute deviation between the GW and SRSH results for the top-most valence band and bottom-most conduction band, over all k points, is 0.060 eV, 0.063 eV, and 0.103 eV for monolayers WS$_2$, WSe$_2$ and MoSe$_2$, respectively, and 0.059 eV, 0.074 eV, and 0.098 eV for the bulk.

We note that the parameter γ is relatively small and similar to the value for MoS$_2$ reported in Ref. [39]. As a consequence, one might be tempted to conclude that the SRSH functional behaves almost as the corresponding limit of a global hybrid [68]. However, in the $\gamma \to 0$ limit, β would be irrelevant and the exchange would be asymptotically screened by $1/\alpha$ instead of ϵ_∞, with consequences for predicted exciton binding energies. For example, in Chen *et al.* [63], the fraction of exact exchange was tuned to fulfill the ionization potential theorem in a system with a defect. It was concluded in that work that using a global hybrid that is tuned to the band gap at only one k point may lead to inaccurate electronic structure predictions.
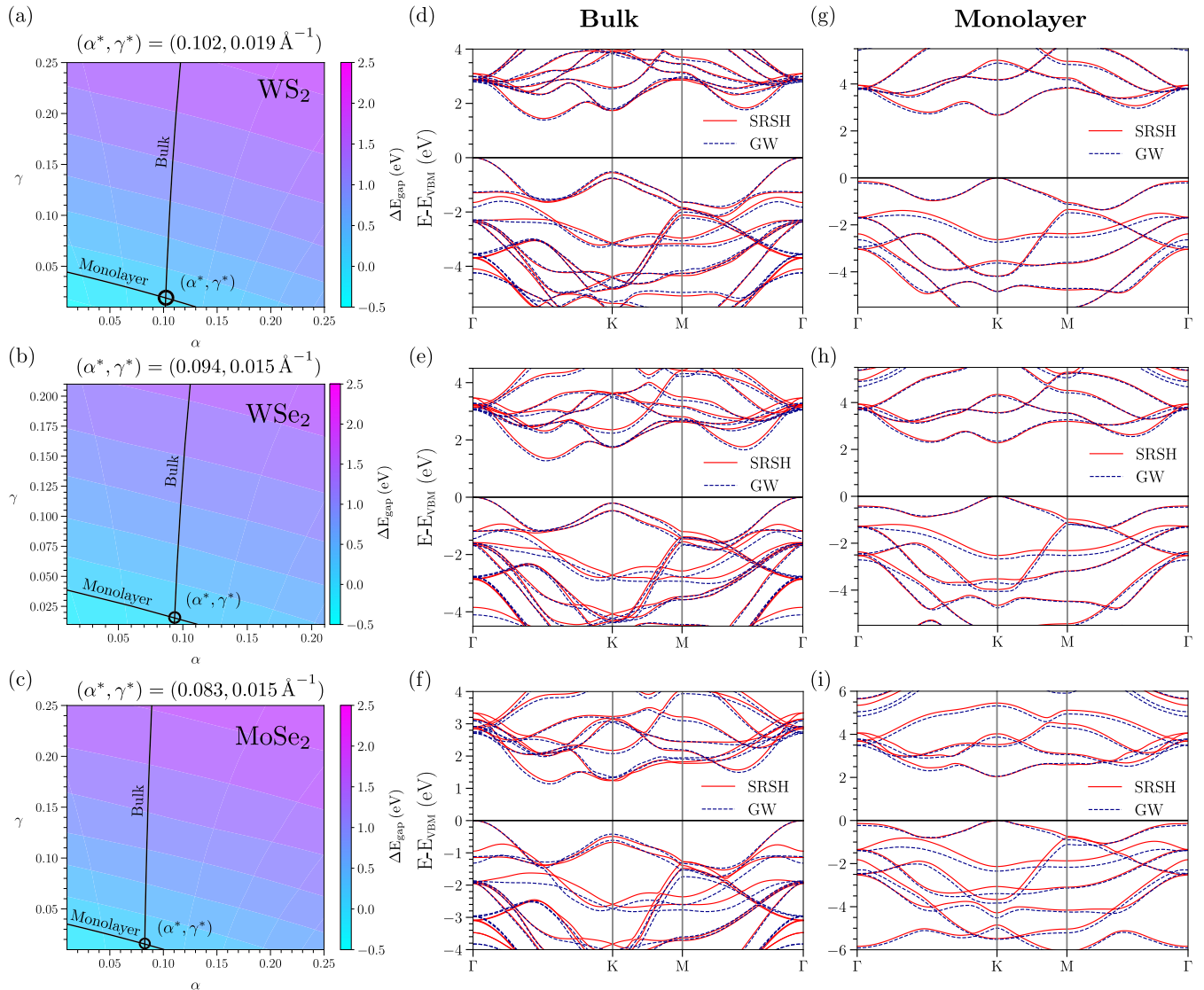
FIG. 1. [(a)–(c)] Contour maps of the gap deviation, ΔE_g, for WS_2, WSe_2, and $MoSe_2$. The solid black lines represent the values for which $\Delta E_g = 0$ for bulk and monolayer structures and the intersection of the two lines yields a unique set of values (α^*, γ^*) that are transferable between the bulk and monolayer. [(d)–(f)] Band structures for bulk and [(g)–(i)] band structures for monolayers of WS_2, WSe_2, and $MoSe_2$ from SRSH (solid lines) and G_0W_0@PBE (dashed lines). Here and throughout, special points in the Brillouin zone are defined explicitly in Sec. S3 of the SM. γ has units of $Å^{-1}$.

This underscores the importance of using a range-separated hybrid rather than a global one.

Next, we consider optical absorption spectra for the same materials, as shown in Fig. 2. These calculations were performed without spin-orbit coupling, primarily due to the computational cost of the reference GW-BSE calculations. Insets provide corresponding TD-SRSH spectra for monolayers that do include spin-orbit coupling. Recalling that SRSH parameters are only tuned to reproduce the GW band gap at a single k point, any further calculations with the same parameters are true tests of the predictive capability of the functional. As seen in Fig. 2, the overall agreement between the GW-BSE and TD-SRSH spectra is highly satisfactory, especially for the low-energy part of the spectrum. At higher energies ($\gtrsim 2.5$ eV), some disagreement becomes apparent, most likely due to the above-noted larger deviations between higher and lower lying SRSH and GW eigenvalues.

Nonetheless, the agreement between GW-BSE and TD-SRSH spectra is particularly good for the bulk and the neglect of the anisotropy of the dielectric constant does not seem to have introduced qualitative failures in the monolayer calculations. For the latter, the positions of the low-energy peaks are generally in good agreement between TD-SRSH and GW-BSE (deviations smaller than 0.1 eV), whereas the discrepancy in peak heights is more apparent.

Upon inclusion of spin-orbit coupling in the SRSH monolayer calculations (insets of Figs. 2(b), 2(d), 2(f)), we observe the appearance of the characteristic A and B excitonic peaks of TMDC monolayers. For WS_2, the experimentally measured A and B peaks are at 2.12 eV and 2.5 eV [69], respectively, which compares excellently to the TD-SRSH peaks located at 2.05 eV and 2.38 eV. Likewise, for WSe_2, the experimental values are 1.74 eV and 2.16 eV [70], compared to TD-SRSH values at 1.70 eV and 1.98 eV, which represent a slightly
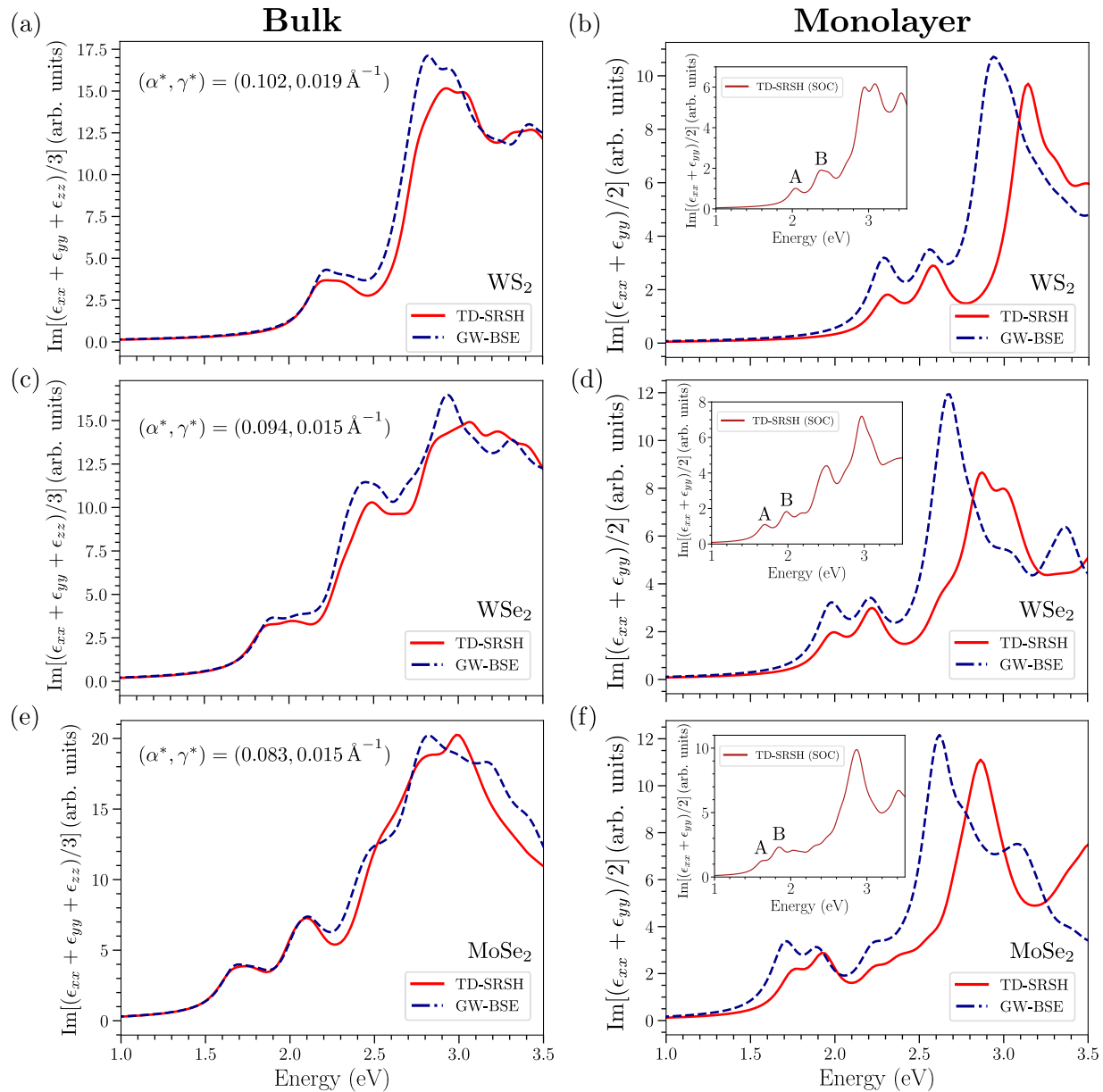
FIG. 2. Optical absorption spectra calculated, without spin-orbit coupling, using TD-SRSH (red solid line) and GW-BSE (blue dashed line). Rows correspond to WS_2, WSe_2, and $MoSe_2$. Results for the bulk and for the monolayer are given in the left and right columns, respectively. Insets: corresponding monolayer SRSH calculations that include spin-orbit coupling, in which the A and B peaks represent excitons of the TMDCs. See Table I for specific parameters.

larger, but still small, deviation. Lastly, for $MoSe_2$, the experimentally measured A and B peaks are at 1.64 eV and 1.83 eV [71], respectively, while the TD-SRSH peaks are located at 1.63 eV and 1.85 eV.

B. Black phosphorus and phosphorene

Among the allotropes of phosphorus, black phosphorus (BP) is one of the most stable forms under ambient conditions [72]. In its ground state, BP is composed of puckered monolayers arranged in an AB stacked structure (space group 64, *Cmce*) and is very sensitive to changes in pressure [73,74]. It is also characterized by strong in-plane anisotropy that provides an opportunity for exploiting its orientation-dependent

optoelectronic properties in a variety of applications [74–76]. The band gap of BP varies from about 0.3 eV in the bulk to around 2.0 eV for the monolayer (phosphorene), covering much of the range between semiconducting TMDCs and gapless graphene [74,75,77].

Because BP is a narrow-gap semiconductor, semilocal functionals such as PBE [78] predict an incorrect metallic ground state for this material, creating a qualitatively incorrect starting point for "single-shot" GW calculations [79–81]. Therefore, here we employed the HSE06 short-range hybrid functional [82,83] to produce a gapped (0.317 eV direct gap at Γ [84]) starting point for the GW calculation. The use of hybrid functionals as a starting point for perturbative GW calculations is a topic of ongoing research (e.g.,
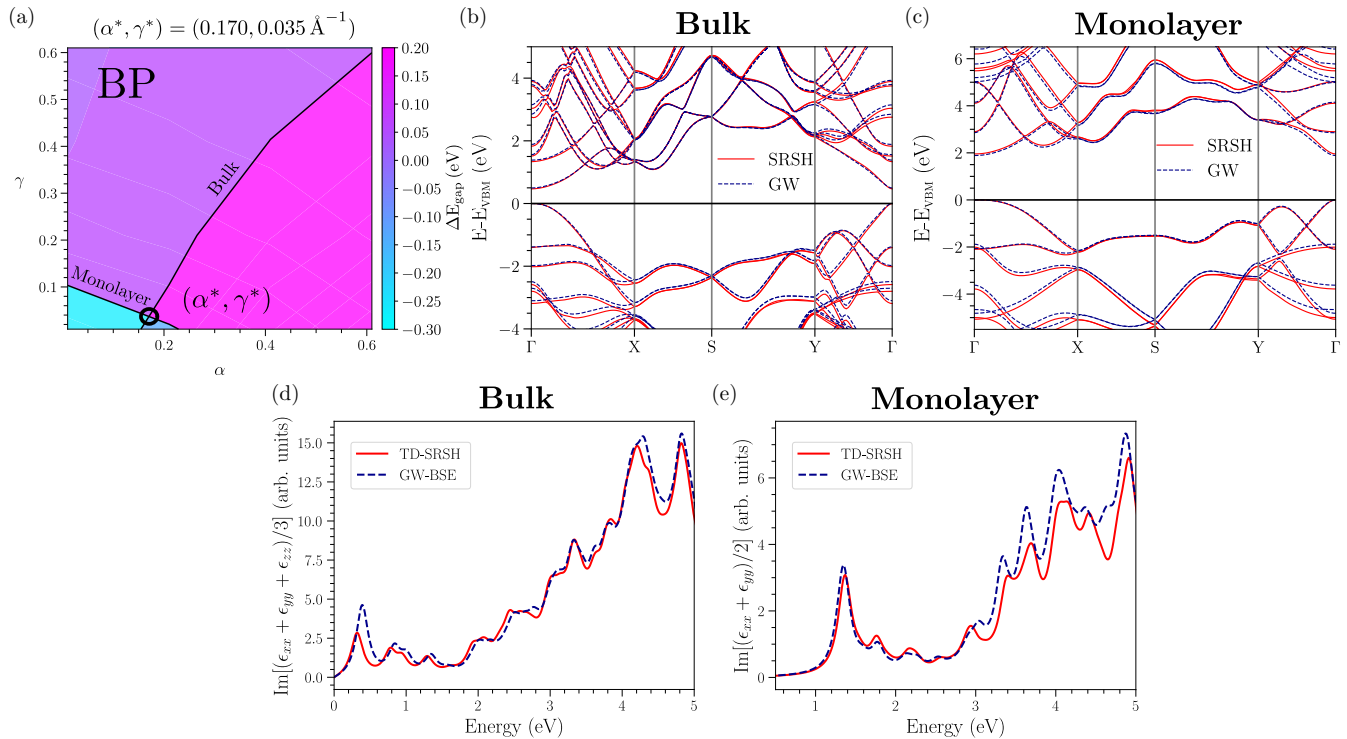
FIG. 3. (a) Gap deviation, ΔE_g, exhibited as a color map in the $\alpha - \gamma$ plane, for black phosphorus. The solid black lines represent the values for which $\Delta E_g = 0$ for bulk and monolayer structures and the intersection of the two lines yields a unique set of values (α^*, γ^*) that are transferable between the bulk and monolayer. (b) Band structures for bulk and (c) monolayer of black phosphorus from SRSH (solid lines) and G_0W_0@HSE06 (dashed lines). (d) Optical absorption spectra for bulk and (e) monolayer of black phosphorus from TD-SRSH (solid red lines) and G_0W_0-BSE (dashed blue lines). γ has units of Å^{-1}.

Refs. [50,81,85–88]). In the present case, this approach yielded a G_0W_0@HSE06 extrapolated band gap of 0.56 eV, in good agreement with Refs. [88,89].

Figure 3(a) displays contour plots of the error, ΔE_g, in the SRSH band gap relative to the GW (G_0W_0@HSE06) fitting target (see SM for details). The zero crossing lines of the ΔE_g surfaces for BP and phosphorene intersect at $(\alpha^*, \gamma^*) = (0.170, 0.035 \text{ Å}^{-1})$, which furnishes the optimal set of parameters for further SRSH/TD-SRSH calculations. The complete set of parameters is listed in Table I.

Using these parameters, Figs. 3(b)–3(e) display corresponding band structures and optical absorption spectra for BP and phosphorene. Once again, owing to the tuning to extrapolated GW band gaps, there is a small deviation between unextrapolated GW and SRSH values, but beyond that, once again we find excellent agreement between the GW and SRSH band structures, both for BP and phosphorene, not just at the band edges but also up to ~2 eV into the valence and conduction bands. Again, the mean absolute deviation for the highest valence band and lowest conduction band across the entire Brillouin zone is a mere 0.054 eV for the bulk phase and 0.071 eV for the monolayer. For the optical spectra, we find excellent agreement between the two approaches, with deviations in peak positions being at most 60 meV in the low-energy part of the spectrum ($\lesssim 2.5$ eV). The first excitonic peak for phosphorene is located at 1.37 eV, in agreement with a previous BSE study [77]. Here, TD-SRSH and GW-BSE peak heights are also in better agreement than for the TMDCs.

C. Indium selenide

As a final example, we consider β-InSe (space group $P6_3/mmc$). This is a transition-metal monochalcogenide that is part of a larger group of similar materials composed of a Group IIIA element (In, Ga) and a chalcogen (S, Se, Te) [90]. This material exhibits a band gap that changes from 2.87 eV (indirect gap) for a monolayer (theoretical) [91] to 1.20–1.28 eV (direct gap) for the bulk [92–94], as well as high-carrier mobility [90,95], making it a desirable candidate for optoelectronics [90,96–98].

Figure 4(a) displays the contour plots of the gap deviation, ΔE_g, in the SRSH band gap relative to the GW fitting targets for the bulk and monolayer structures (see Sec. S2 of the SM). Similar to the TMDCs, we observe that the bulk phase exhibits a very small degree of acceptable variation in the fraction of short-range exact exchange, α, whereas this parameter can vary more widely for the monolayer. The optimal set of SRSH parameters, $(\alpha^*, \gamma^*) = (0.149, 0.021 \text{ Å}^{-1})$, is again obtained from the point of intersection of the zero-crossing lines of the ΔE_g surfaces for bulk and monolayer InSe. The complete set of parameters for InSe is listed in Table I. Using this tuned SRSH functional, Figs. 4(b) and 4(c) show the band structures of bulk and monolayer InSe, along with reference band structures from GW calculations. Once again, owing to extrapolation the SRSH gaps differ from the GW ones by 60 meV for the bulk and 30 meV for the monolayer. As seen in the figure, the agreement between the SRSH and GW band structures is quite satisfactory across the chosen
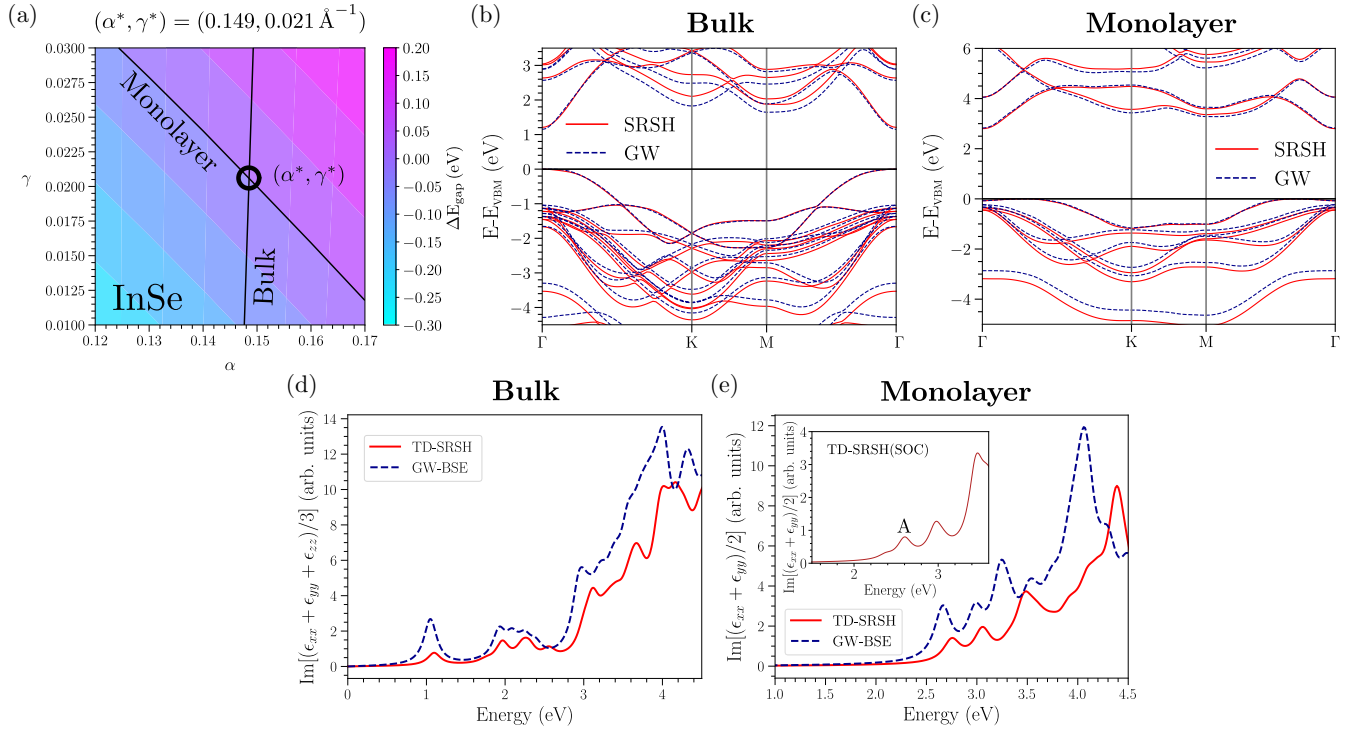
FIG. 4. (a) Gap deviation, ΔE_g, exhibited as a color map in the $\alpha - \gamma$ plane, for InSe. The solid black lines represent the values for which $\Delta E_g = 0$ for bulk and monolayer structures and the intersection of the two lines yields a unique set of values (α^*, γ^*) that are transferable between the bulk and monolayer. (b) Band structures for bulk and (c) monolayer of InSe from SRSH (solid lines) and G_0W_0@PBE (dashed lines). (d) Optical absorption spectra for bulk and (e) monolayer of InSe from TD-SRSH (solid red lines) and G_0W_0-BSE (dashed blue lines). Inset: TD-SRSH calculation with SOC. γ has units of Å^{-1}.

high-symmetry paths, with a mean absolute deviation for the top valence band and the bottom conduction band of 0.163 eV for the bulk and 0.085 eV for the monolayer.

TD-SRSH optical absorption spectra for bulk and monolayer InSe are displayed in Figs. 4(d) and 4(e), along with reference GW-BSE spectra. The TD-SRSH and GW-BSE spectra are in good agreement below ~3 eV, with the largest error in the energies of the first two peaks being of the order of 0.2 eV, albeit with some differences in the oscillator strength. The agreement between the TD-SRSH and GW-BSE optical spectra is not as good above 3 eV. The remaining discrepancies may be partly due to computational limitations in k-point sampling in the GW calculations. The inset of Fig. 4(e)

displays the TD-SRSH absorption spectrum for the monolayer with the inclusion of spin-orbit coupling; the first excitonic peak (labeled A) appears at 2.6 eV and agrees well with the value of 2.57 eV obtained from Ref. [99].

IV. ASSESSMENT OF SRSH FUNCTIONALS FOR BILAYER MoS$_2$ AND h-BN

Motivated by the promising results of the SRSH/TD-SRSH approach for bulk and monolayer structures, we now seek to understand how well these functionals perform for bilayers of vdW materials. In general, one could expect that as long as the characteristic length scale for switching

TABLE II. Brillouin zone grid, tuned SRSH parameters (α^*, γ^*) for bulk monolayer, tuned SRSH parameters (α', γ') for bulk bilayer, average inverse macroscopic dielectric constant (ϵ_∞^{-1}), GW band gap (E^{GW}), GW-BSE optical gap (E_{opt}^{GW-BSE}), SRSH band gap $(E^{SRSH}$, fitted to an extrapolated GW quasiparticle band gap), and TD-SRSH optical gap $(E_{opt}^{TD-SRSH})$ for MoS$_2$ and h-BN. Additional computational details for the calculations are given in Secs. S1-S3 of the SM. Band gaps and optical gaps are calculated at the K point for all phases.

Material	Phase	**k** grid	α^*	γ^* (Å^{-1})	α'	γ' (Å^{-1})	ϵ_∞^{-1}	E^{GW} (eV)	E_{opt}^{GW-BSE} (eV)	E^{SRSH} (eV)	$E_{opt}^{TD-SRSH}$ (eV)
MoS$_2$	Bulk	$12 \times 12 \times 4$[a]					0.085	2.07[a]	2.00[a]	2.03[a]	1.91
	2L	$15 \times 15 \times 1$	0.107	0.038	0.105	0.008	1.0	2.20	1.90	2.18	1.97
	1L	$18 \times 18 \times 1$[a]					1.0	2.50[a]	2.00[a]	2.65[a]	2.02
h-BN	Bulk	$12 \times 12 \times 4$[a]					0.25	6.58[a]	5.48[a]	6.66[a]	5.82
	2L	$18 \times 18 \times 1$	0.201	0.072	0.204	0.041	1.0	6.79	5.29	6.95	5.91
	1L	$18 \times 18 \times 1$[a]					1.0	7.20[a]	5.31[a]	7.26[a]	5.92

[a]From Ref. [39].

from short-range exact exchange (α) to long-range exact exchange ($1/\epsilon_\infty$), namely $1/\gamma$, is greater than the thickness (t) of the bilayer/few-layer slab, the interaction between two charges separated across the slab thickness will be governed largely by the (tuned) short-range exchange. In this scenario, it is reasonable to hypothesize that the SRSH/TD-SRSH formalism ought to retain its accuracy for bilayer/few-layer structures, even when merely employing the simply functional form of the SRSH with asymptotic long-range screening of $\epsilon_\infty = 1$. In the following, we test this hypothesis for bilayer MoS$_2$ and h-BN, bulk and monolayers of which were studied previously in Ref. [39].

A. MoS$_2$

Tuned SRSH parameters, (α^*, γ^*), for bulk and monolayer MoS$_2$ were reported previously in Ref. [39] and are listed in Table II. In principle, one could use these parameters directly to make a *prediction* for bilayer MoS$_2$. It is also possible to retune the SRSH using bilayer MoS$_2$ and the bulk as reference structures. To this end, we first perform GW calculations for MoS$_2$ bilayers to determine the reference quasiparticle band gaps (see Sec. S2 of the SM and Table II). We then apply our tuning procedure (Sec. II) to obtain the error, ΔE_g, for the bilayer as a function of α and γ. Figure 5(a) displays the ΔE_g contour plots for monolayer, bilayer, and bulk MoS$_2$. As seen in the figure, the optimal parameters for the bilayer and bulk, labeled α' and γ', are not identical to those of the monolayer and bulk (α^*, γ^*). Specifically, α' and α^* do not vary substantially, as the bulk constrains these values to a rather small window, and the main distinction is manifested in the values of γ' and γ^*. In addition, the ΔE_g surfaces of the monolayer and bilayer and, consequently, the zero-crossing lines are nearly parallel to each other. This indicates that it is not possible to render $\Delta E_g = 0$ simultaneously for the monolayer and bilayer, though this does not rule out simultaneous minimization of a different metric, an issue we do not explore further here.

Figures 5(b) and 5(c) display the SRSH band structure and TD-SRSH optical absorption spectrum for bilayer MoS$_2$, using the optimal values of α' and γ', along with their GW and GW-BSE counterparts. As before, there is an intrinsic 20 meV extrapolation difference. The overall agreement between the two approaches is excellent: the mean absolute error in the energy eigenvalues, considering the lowermost conduction band and the uppermost valence band, is a mere 0.087 eV. Similarly, we also find good agreement between the GW-BSE and TDSRSH optical spectra [Fig. 5(c)] with differences of less than 0.1 eV in peak positions for the low-energy part of the spectrum ($\lesssim 2.5$ eV). The inset of Fig. 5(c) displays the TD-SRSH absorption spectrum with spin-orbit coupling included. We observe the characteristic splitting of the valence band into A and B excitonic peaks at 1.88 eV and 2.23 eV, respectively, that are in excellent agreement with the reported experimental values of 1.91 eV (A peak) and 2.12 eV (B peak) [100].

Returning to the issue of the transferability of the SRSH functional, we sought to understand the implications of modeling the MoS$_2$ bilayer using a functional specifically tuned for the monolayer and bulk (parameters α^* and γ^*) and,
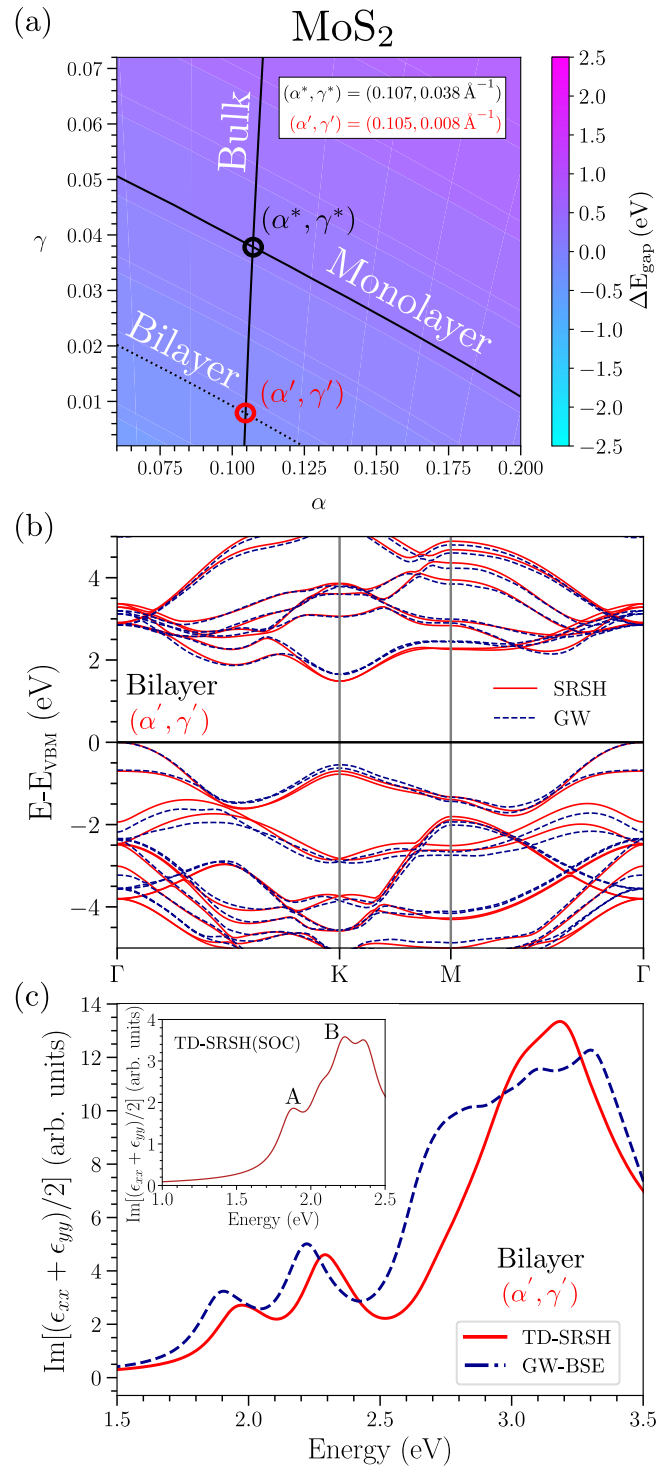

FIG. 5. (a) 2D contour plots of the gap deviation, ΔE_g, for monolayer, bilayer, and bulk MoS$_2$. Solid black lines represent values for which $\Delta E_g = 0$. The intersections of the solid lines yield a set of values (α^*, γ^*) that are transferable between the monolayer and bulk and a somewhat different set of values (α', γ') that are transferable between the bilayer and bulk. (b) Band structures for bilayer MoS$_2$ from SRSH (red solid lines), using the parameters (α', γ'), and from G_0W_0@local density approximation (G_0W_0@LDA, blue dashed lines). (c) Optical absorption spectra for bilayer MoS$_2$ obtained with TD-SRSH (red solid line) and GW-BSE (blue dashed line). Inset: TD-SRSH calculation with SOC. γ has units of Å^{-1}.
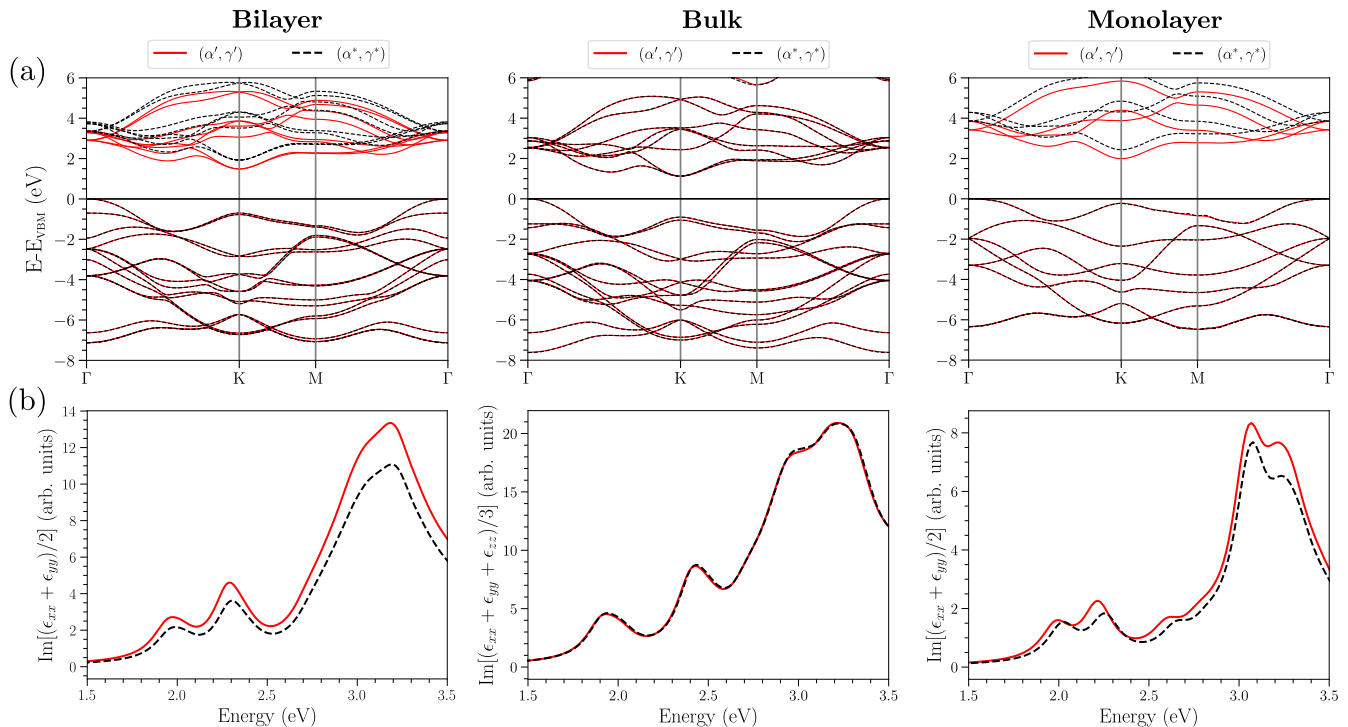
FIG. 6. (a) Band structures of MoS$_2$ in the bilayer, bulk, and monolayer phases, calculated using the parameters indicated in Table II and with $(\alpha^*, \gamma^*) = (0.107, 0.038 \text{ Å}^{-1})$ and $(\alpha', \gamma') = (0.105, 0.008 \text{ Å}^{-1})$, obtained from the intersections between zero crossings indicated in Fig. 5. The former pair is optimal for the monolayer and the latter for the bilayer. The choice of optimal versus nonoptimal parameters leads to a near constant error of ~0.5 eV in band gaps along the indicated high-symmetry **k** path for bilayer and monolayer. The band structure of the bulk is not sensitive to the choice of optimal parameters. (b) Optical absorption spectra for the phases and band structures in (a).

conversely, modeling the monolayer using a functional specifically tuned for the bilayer and bulk (parameters α' and γ'). Figure 6(a) presents the outcome of such a comparison for the bilayer, bulk, and monolayer, with Fig. 6(b) displaying the corresponding TD-SRSH spectra. For the bulk structure, we find that the band structure and optical spectrum is essentially insensitive to the choice of parameters, as may be expected given that both sets of values are optimal for bulk MoS$_2$ ($\Delta E_g = 0$). For the monolayer and bilayer, using the nonoptimal set of parameters leads to nearly rigid shifts of the band structure by ~0.5 eV. The optical absorption spectra display lower sensitivity to this choice of parameters. For the bilayer, the only noteworthy change is in the amplitudes of the spectral features, whereas for the monolayer the differences in the energies of the spectral features (~0.1 eV) is somewhat more noticeable. Thus use of nonoptimal parameters, (α^*, γ^*), for the bilayer will overestimate exciton binding energies by ~0.5 eV. Mitigating these errors may require a more complex multiobjective error function or the development of alternative dielectric screening models that explicitly account for the thickness of the two-dimensional (2D) layer/slab [101–103].

B. h-BN

The tuned SRSH parameters, (α^*, γ^*), for bulk and monolayer h-BN were reported in Ref. [39] and are listed in Table II. Following the same tuning procedure, we first perform GW calculations to determine the reference quasiparticle band gaps for h-BN bilayers (see Sec. S2 of the SM and Table II).

Figure 7(a) exhibits ΔE_g contour plots for monolayer, bilayer, and bulk h-BN. Also in this case, the optimal parameters for the bilayer and bulk, labeled α' and γ', are not identical to those optimized for the monolayer and bulk (α^*, γ^*), differing mostly in the range-separation parameter γ. The SRSH band structure for the bilayer is displayed in Fig. 7(b), along with the reference GW calculation. Here the extrapolation difference is 160 meV. The two results are in good agreement. Considering the lowermost conduction band and the uppermost valence band, the mean absolute error is 0.207 eV. The TD-SRSH spectrum for the bilayer is displayed in Fig. 7(c), along with the reference GW-BSE spectrum. Clearly, the former is blueshifted by approximately 0.6 eV relative to the latter. This is a known issue, discussed previously in Ref. [39], and it is not pursued further here.

Finally, in Fig. 8 we assess the transferability of the parameters (α^*, γ^*) and (α', γ') between monolayer, bilayer, and bulk h-BN, as done in Fig. 6 for MoS$_2$. For bulk h-BN, the band structure and optical spectrum is insensitive to the choice of parameters. For the monolayer and bilayer, in contrast, using the nonoptimal set of parameters leads to nearly rigid shifts of the band structure by ~0.35 eV. We also display in Fig. 8 the TD-SRSH absorption spectra for the monolayer and bilayer using the two different sets of parameters for α and γ. Noting that the absorption spectrum suffers from a large blueshift, as discussed above, we only seek to understand *relative* differences between the TD-SRSH spectra. For both monolayer and bilayer h-BN, the position of the first excitonic peak changes only slightly by about 0.03 eV and the
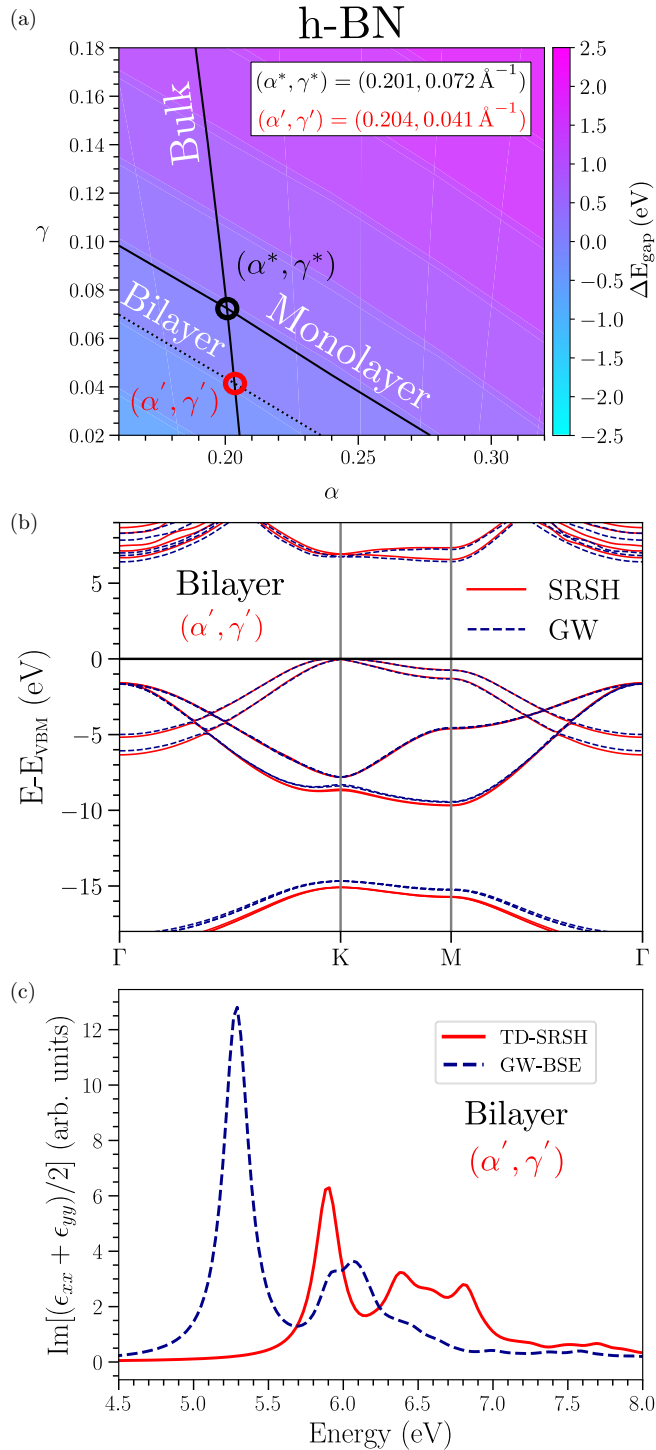
FIG. 7. (a) 2D contour plots of the gap deviation, ΔE_g, for monolayer, bilayer, and bulk h-BN. The solid black lines represent the values for which $\Delta E_g = 0$ for these structures. The intersections of the solid lines yield a set of values (α^*, γ^*) that are transferable between the monolayer and bulk and another set of values (α', γ') that are transferable between the bilayer and bulk. (b) Band structures for bilayer h-BN from SRSH (solid lines), using the parameters (α', γ'), and G_0W_0@local density approximation (G_0W_0@LDA, blue dashed lines). (c) Optical absorption spectra for bilayer h-BN obtained with TD-SRSH (solid line) and GW-BSE (dashed line). γ has units of $Å^{-1}$.

peak heights are also only slightly affected. The exciton binding energy, however, does not change by the same amount. This may be attributed to the approximation of $\epsilon_\infty = 1.0$ for the bilayer, showing a limitation of this approximation in the case of the bilayer phases. Beyond the first peak though, the absorption spectra show more significant changes with the appearance of additional satellite peaks and/or shoulders. It is therefore likely that the comparison between GW-BSE and TD-SRSH for h-BN (and possibly other large-gap layered insulators) needs to be revisited, which is an issue we will take up elsewhere.

V. CONCLUSION

In conclusion, we have demonstrated a facile approach for the construction of transferable SRSH functionals for bulk and mono-/bilayer vdW materials. By tuning the SRSH functional to reproduce just one (GW) quasiparticle energy, we have demonstrated the ability to achieve excellent agreement between SRSH and GW band structures of bulk and mono-/bilayers TMDCs, black phosphorus, InSe, and h-BN, at a fraction of the computational cost of GW calculations. We have also shown that TD-SRSH calculations of excited-state properties, which do not enter at any stage into the functional tuning procedure, are generally in good agreement with the BSE approach, thus lending credence to the predictive capability of the SRSH/TD-SRSH formalism. The one exception to this finding is h-BN, the optical spectra of which are at variance with their BSE counterparts. As no such deviations have been reported before for SRSH studies of bulk insulators [37], it remains to be understood if this is a generic problem posed by large-gap 2D insulators which manifests in all phases of such materials and, if so, how to incorporate missing physical effects into the SRSH exchange-correlation kernel. Furthermore, more research must be carried out in the case of few-layered materials, where the approximation $\epsilon_\infty = 1.0$ may present limitations in capturing some physical properties quantitatively.

One difficulty arises if the exciton binding energy is very small. The expected level of agreement between GW and SRSH, and also between GW-BSE and TD-SRSH, is of the order of 0.1–0.15 eV. This is usually within the experimental accuracy of the measurements and also results in errors much smaller than the value itself, either for the band gap energy and the optical gap. An error of 0.1 eV, which is an excellent outcome in itself, can still lead to a 50% error in the exciton binding energy. For the case of small band gap materials, for example, BP, the error may be even bigger. Therefore, interpretation of exciton binding energies should be performed with caution.

Our results suggest that the SRSH/TD-SRSH approach is robust for 2D semiconductors, opening up a range of opportunities for accurate calculations of the optoelectronic properties of layered materials with defects, heterolayers/-junctions, twisted or shifted layers, and more.
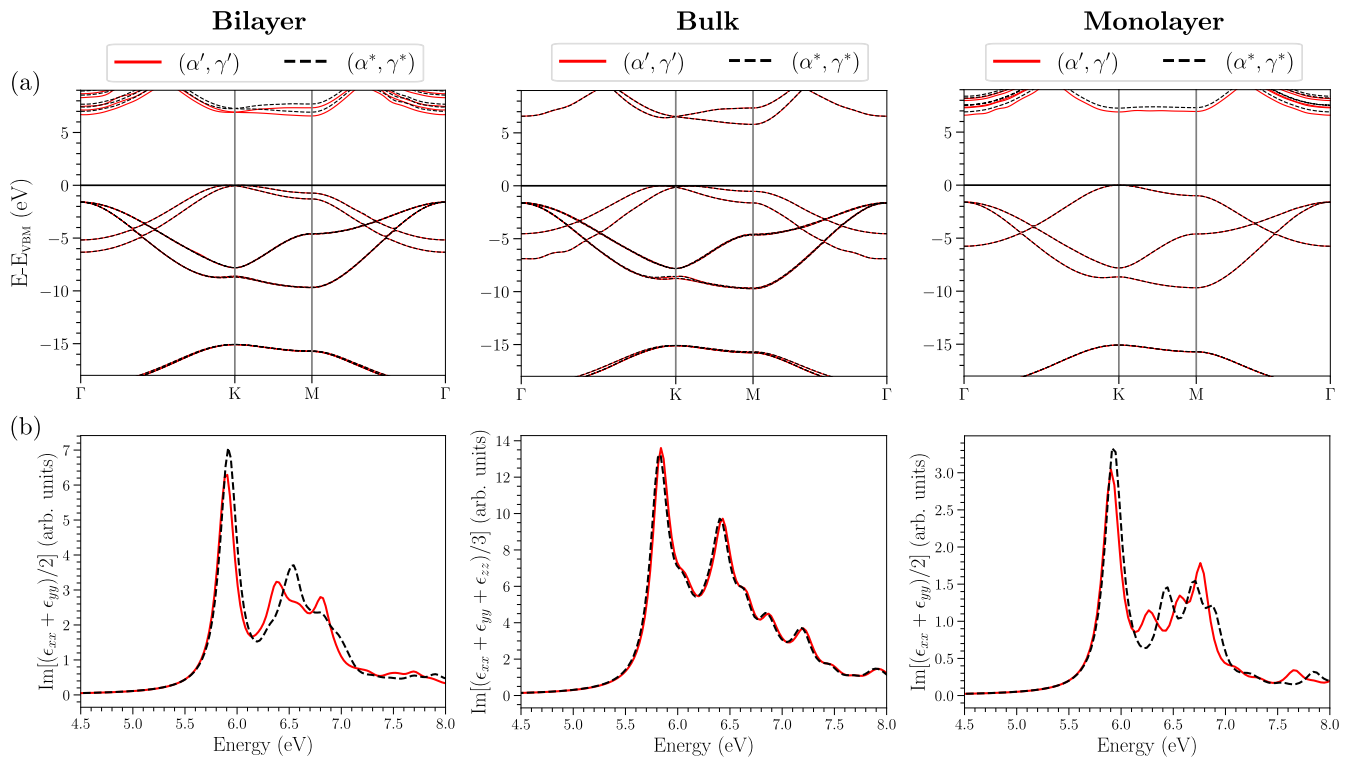
ACKNOWLEDGMENTS

FIG. 8. (a) Band structures of h-BN in the bilayer, bulk, and monolayer phases, calculated using the parameters indicated in Table II and with $(\alpha^*, \gamma^*) = (0.201, 0.072 \text{ Å}^{-1})$ and $(\alpha', \gamma') = (0.204, 0.041 \text{ Å}^{-1})$, obtained from the intersections between zero crossings indicated in Fig. 7. The former pair is optimal for the monolayer and the latter for the bilayer. The choice of optimal versus nonoptimal parameters leads to a near constant error of ~ 0.35 eV in band gaps along the indicated high-symmetry **k** path for bilayer and monolayer. The band structure of the bulk is not sensitive to the choice of optimal parameters. (b) Optical absorption spectra for the phases and band structures in (a).

[1] A. K. Geim and I. V. Grigorieva, Van der Waals heterostructures, Nature (London) **499**, 419 (2013).

[2] K. S. Novoselov, A. Mishchenko, A. Carvalho, and A. H. C. Neto, 2D materials and van der Waals heterostructures, Science **353**, aac9439 (2016).

[3] P. M. Ajayan, P. Kim, and K. Banerjee, Two-dimensional van der Waals materials, Phys. Today **69**(9), 38 (2016).

[4] K. S. Novoselov, A. K. Geim, S. V. Morozov, D. Jiang, Y. Zhang, S. V. Dubonos, I. V. Grigorieva, and A. A. Firsov, Electric field effect in atomically thin carbon films, Science **306**, 666 (2004).

[5] K. S. Novoselov, D. Jiang, F. Schedin, T. J. Booth, V. V. Khotkevich, S. V. Morozov, and A. K. Geim, Two-dimensional atomic crystals, Proc. Natl. Acad. Sci. USA **102**, 10451 (2005).

[6] Y. Liu, N. O. Weiss, X. Duan, H.-C. Cheng, Y. Huang, and X. Duan, Van der waals heterostructures and devices, Nat. Rev. Mater. **1**, 16042 (2016).

[7] L. Balents, C. R. Dean, D. K. Efetov, and A. F. Young, Superconductivity and strong correlations in moiré flat bands, Nat. Phys. **16**, 725 (2020).

[8] E. Y. Andrei, D. K. Efetov, P. Jarillo-Herrero, A. H. MacDonald, K. F. Mak, T. Senthil, E. Tutuc, A. Yazdani, and A. F. Young, The marvels of moiré materials, Nat. Rev. Mater. **6**, 201 (2021).

[9] F. He, Y. Zhou, Z. Ye, S.-H. Cho, J. Jeong, X. Meng, and Y. Wang, Moiré patterns in 2D materials: A review, ACS Nano **15**, 5944 (2021).

[10] M. Vizner Stern, Y. Waschitz, W. Cao, I. Nevo, K. Watanabe, T. Taniguchi, E. Sela, M. Urbakh, O. Hod, and M. Ben Shalom,

Interfacial ferroelectricity by van der Waals sliding, Science **372**, 1462 (2021).

[11] S. Deb, W. Cao, N. Raab, K. Watanabe, M. Goldstein, L. Kronik, M. Urbakh, O. Hod, and M. Ben Shalom, Cumulative polarization in conductive interfacial ferroelectrics, Nature (London) **612**, 465 (2022).

[12] A. Castellanos-Gomez, X. Duan, Z. Fei, H. R. Gutierrez, Y. Huang, X. Huang, J. Quereda, Q. Qian, E. Sutter, and P. Sutter, Van der waals heterostructures, Nat. Rev. Methods Primers **2**, 58 (2022).

[13] L. Hedin, New method for calculating the one-particle green's function with application to the electron-gas problem, Phys. Rev. **139**, A796 (1965).

[14] G. Onida, L. Reining, and A. Rubio, Electronic excitations: density-functional versus many-body Green's-function approaches, Rev. Mod. Phys. **74**, 601 (2002).

[15] M. S. Hybertsen and S. G. Louie, Electron correlation in semiconductors and insulators: Band gaps and quasiparticle energies, Phys. Rev. B **34**, 5390 (1986).

[16] M. Rohlfing and S. G. Louie, Electron-hole excitations in semiconductors and insulators, Phys. Rev. Lett. **81**, 2312 (1998).

[17] S. Albrecht, L. Reining, R. Del Sole, and G. Onida, *Ab initio* calculation of excitonic effects in the optical spectra of semiconductors, Phys. Rev. Lett. **80**, 4510 (1998).

[18] D. Y. Qiu, F. H. da Jornada, and S. G. Louie, Optical spectrum of MoS_2: Many-body effects and diversity of exciton states, Phys. Rev. Lett. **111**, 216805 (2013).

[19] D. Y. Qiu, F. H. da Jornada, and S. G. Louie, Erratum: Optical spectrum of MoS_2: Many-body effects and diversity of exciton states [Phys. Rev. Lett. **111**, 216805 (2013)], Phys. Rev. Lett. **115**, 119901(E) (2015).

[20] J. Liu, Z. Li, X. Zhang, and G. Lu, Unraveling energy and charge transfer in type-II van der Waals heterostructures, npj Comput. Mater. **7**, 191 (2021).

[21] M. Bernardi, C. Ataca, M. Palummo, and J. C. Grossman, Optical and electronic properties of two-dimensional layered materials, Nanophotonics **6**, 479 (2017).

[22] C. Attaccalite, M. S. Prete, M. Palummo, and O. Pulci, Interlayer and intralayer excitons in AlN/WS_2 heterostructure, Materials **15**, 8318 (2022).

[23] L. Xu, M. Yang, S. J. Wang, and Y. P. Feng, Electronic and optical properties of the monolayer group-IV monochalcogenides MX (M = Ge, Sn; X = S, Se, Te), Phys. Rev. B **95**, 235434 (2017).

[24] M. Govoni and G. Galli, Large scale GW calculations, J. Chem. Theory Comput. **11**, 2680 (2015).

[25] D. Golze, M. Dvorak, and P. Rinke, The gw compendium: A practical guide to theoretical photoemission spectroscopy, Front. Chem. **7**, 377 (2019).

[26] M. Del Ben, F. H. da Jornada, A. Canning, N. Wichmann, K. Raman, R. Sasanka, C. Yang, S. G. Louie, and J. Deslippe, Large-scale GW calculations on pre-exascale HPC systems, Comput. Phys. Commun. **235**, 187 (2019).

[27] R. G. Parr and W. Yang, *Density Functional Theory of Atoms and Molecules* (Oxford University Press, Oxford, 1989).

[28] M. Dreizler and E. K. U. Gross, *Density Functional Theory: An Approach to the Quantum Many-Body Problem* (Springer, Berlin, 1990).

[29] C. A. Ullrich, *Time-Dependent Density-Functional Theory: Concepts and Applications* (Oxford University Press, Oxford, 2011).

[30] M. A. L. Marques, N. T. Maitra, F. M. S. Nogueira, E. K. U. Gross, and A. Rubio, *Fundamentals of Time-Dependent Density-Functional Theory* (Springer, Heidelberg, 2012).

[31] L. Kronik and J. B. Neaton, Excited-state properties of molecular solids from first principles, Annu. Rev. Phys. Chem. **67**, 587 (2016).

[32] L. Kronik and S. Kümmel, Dielectric screening meets optimally tuned density functionals, Adv. Mater. **30**, 1706560 (2018).

[33] M. Gerosa, C. E. Bottani, L. Caramella, G. Onida, C. Di Valentin, and G. Pacchioni, Electronic structure and phase stability of oxide semiconductors: Performance of dielectric-dependent hybrid functional DFT, benchmarked against *GW* band structure calculations and experiments, Phys. Rev. B **91**, 155201 (2015).

[34] A. Tal, P. Liu, G. Kresse, and A. Pasquarello, Accurate optical spectra through time-dependent density functional theory based on screening-dependent hybrid functionals, Phys. Rev. Res. **2**, 032019(R) (2020).

[35] S. Refaely-Abramson, S. Sharifzadeh, M. Jain, R. Baer, J. B. Neaton, and L. Kronik, Gap renormalization of molecular crystals from density-functional theory, Phys. Rev. B **88**, 081204(R) (2013).

[36] D. Lüftner, S. Refaely-Abramson, M. Pachler, R. Resel, M. G. Ramsey, L. Kronik, and P. Puschnig, Experimental and theoretical electronic structure of quinacridone, Phys. Rev. B **90**, 075204 (2014).

[37] S. Refaely-Abramson, M. Jain, S. Sharifzadeh, J. B. Neaton, and L. Kronik, Solid-state optical absorption from optimally tuned time-dependent range-separated hybrid density functional theory, Phys. Rev. B **92**, 081204(R) (2015).

[38] D. Wing, J. B. Haber, R. Noff, B. Barker, D. A. Egger, A. Ramasubramaniam, S. G. Louie, J. B. Neaton, and L. Kronik, Comparing time-dependent density functional theory with many-body perturbation theory for semiconductors: Screened range-separated hybrids and the GW plus Bethe-Salpeter approach, Phys. Rev. Mater. **3**, 064603 (2019).

[39] A. Ramasubramaniam, D. Wing, and L. Kronik, Transferable screened range-separated hybrids for layered materials: The cases of MoS_2 and h-BN, Phys. Rev. Mater. **3**, 084007 (2019).

[40] D. Wing, J. B. Neaton, and L. Kronik, Time-dependent density functional theory of narrow band gap semiconductors using a screened range-separated hybrid functional, Adv. Theory Sim. **3**, 2000220 (2020).

[41] D. Wing, G. Ohad, J. B. Haber, M. R. Filip, S. E. Gant, J. B. Neaton, and L. Kronik, Band gaps of crystalline solids from Wannier-localization based optimal tuning of a screened range-separated hybrid functional, Proc. Natl. Acad. Sci. USA **118**, e2104556118 (2021).

[42] G. Ohad, D. Wing, S. E. Gant, A. V. Cohen, J. B. Haber, F. Sagredo, M. R. Filip, J. B. Neaton, and L. Kronik, Band gaps of halide perovskites from a wannier-localized optimally tuned screened range-separated hybrid, Phys. Rev. Mater. **6**, 104606 (2022).

[43] L.-y. Huang, X. Zhang, M. Zhang, and G. Lu, Effect of point defects on optical properties of graphene fluoride: A first-principles study, J. Phys. Chem. C **121**, 12855 (2017).

[44] J. Liu, X. Zhang, and G. Lu, Excitonic effect drives ultrafast dynamics in van der Waals heterostructures, Nano Lett. **20**, 4631 (2020).

[45] L. Zhang, X. Zhang, and G. Lu, Intramolecular band alignment and spin–orbit coupling in two-dimensional halide perovskites, J. Phys. Chem. Lett. **11**, 6982 (2020).

[46] H. Guo, X. Zhang, and G. Lu, Moiré excitons in defective van der waals heterostructures, Proc. Natl. Acad. Sci. USA **118**, e2105468118 (2021).

[47] J. Krumland and C. Cocchi, Electronic structure of low-dimensional inorganic/organic interfaces: Hybrid density functional theory, G_0W_0, and electrostatic models, Phys. Status Solidi A **2023**, 2300089 (2023).

[48] H. Guo, X. Zhang, and G. Lu, Tuning moiré excitons in janus heterobilayers for high-temperature Bose-Einstein condensation, Sci. Adv. **8**, eabp9757 (2022).

[49] Q. Zhou, Z.-F. Liu, T. J. Marks, and P. Darancet, Range-separated hybrid functionals for mixed dimensional heterojunctions: Application to phthalocyanines/MoS_2, APL Mater. **9**, 121112 (2021).

[50] S. E. Gant, J. B. Haber, M. R. Filip, F. Sagredo, D. Wing, G. Ohad, L. Kronik, and J. B. Neaton, Optimally tuned starting point for single-shot GW calculations of solids, Phys. Rev. Mater. **6**, 053802 (2022).

[51] T. Leininger, H. Stoll, H.-J. Werner, and A. Savin, Combining long-range configuration interaction with short-range density functionals, Chem. Phys. Lett. **275**, 151 (1997).

[52] T. Yanai, D. P. Tew, and N. C. Handy, A new hybrid exchange-correlation functional using the Coulomb-attenuating method (CAM-B3LYP), Chem. Phys. Lett. **393**, 51 (2004).

[53] K. Andersen, S. Latini, and K. S. Thygesen, Dielectric genome of van der Waals heterostructures, Nano Lett. **15**, 4616 (2015).

[54] D. Y. Qiu, F. H. da Jornada, and S. G. Louie, Screening and many-body effects in two-dimensional crystals: Monolayer MoS_2, Phys. Rev. B **93**, 235435 (2016).

[55] M. A. Rohrdanz, K. M. Martins, and J. M. Herbert, A long-range-corrected density functional that performs well for both ground-state properties and time-dependent density functional theory excitation energies, including charge-transfer excited states, J. Chem. Phys. **130**, 054112 (2009).

[56] P. Ghosez, X. Gonze, and R. W. Godby, Long-wavelength behavior of the exchange-correlation kernel in the Kohn-Sham theory of periodic systems, Phys. Rev. B **56**, 12811 (1997).

[57] A. Seidl, A. Görling, P. Vogl, J. A. Majewski, and M. Levy, Generalized Kohn-Sham schemes and the band-gap problem, Phys. Rev. B **53**, 3764 (1996).

[58] S. Kümmel and L. Kronik, Orbital-dependent density functionals: Theory and applications, Rev. Mod. Phys. **80**, 3 (2008).

[59] R. Baer, E. Livshits, and U. Salzner, Tuned range-separated hybrids in density functional theory, Annu. Rev. Phys. Chem. **61**, 85 (2010).

[60] L. Kronik, T. Stein, S. Refaely-Abramson, and R. Baer, Excitation gaps of finite-sized systems from optimally tuned range-separated hybrid functionals, J. Chem. Theory Comput. **8**, 1515 (2012).

[61] M. Gajdoš, K. Hummer, G. Kresse, J. Furthmüller, and F. Bechstedt, Linear optical properties in the projector-augmented wave methodology, Phys. Rev. B **73**, 045112 (2006).

[62] See Supplemental Material at http://link.aps.org/supplemental/10.1103/PhysRevMaterials.7.104001 for computational details, convergence calculations, atomic geometries, comparison with existing literature, and additional results. It includes Refs. [106–126].

[63] W. Chen, S. M. Griffin, G.-M. Rignanese, and G. Hautier, Nonunique fraction of fock exchange for defects in two-dimensional materials, Phys. Rev. B **106**, L161107 (2022).

[64] M. E. Casida, Time-dependent density functional response theory of molecular systems: Theory, computational methods, and functionals, Recent Developments and Applications of Modern Density Functional Theory, in *Theoretical and Computational Chemistry* (Elsevier, Amsterdam, 1996), Vol. 4, pp. 391–439.

[65] T. Sander, E. Maggio, and G. Kresse, Beyond the tamm-dancoff approximation for extended systems using exact diagonalization, Phys. Rev. B **92**, 045209 (2015).

[66] S. Refaely-Abramson, S. Sharifzadeh, N. Govind, J. Autschbach, J. B. Neaton, R. Baer, and L. Kronik, Quasiparticle spectra from a nonempirical optimally tuned range-separated hybrid density functional, Phys. Rev. Lett. **109**, 226405 (2012).

[67] L. Kronik and S. Kümmel, Gas-phase valence-electron photoemission spectroscopy using density functional theory, in *First Principles Approaches to Spectroscopic Properties of Complex Materials*, edited by C. Di Valentin, S. Botti, and M. Cococcioni (Springer, Berlin, 2014), pp. 137–191.

[68] C. Adamo and V. Barone, Toward reliable density functional methods without adjustable parameters: The PBE0 model, J. Chem. Phys. **110**, 6158 (1999).

[69] B. Zhu, X. Chen, and X. Cui, Exciton binding energy of monolayer WS_2, Sci. Rep. **5**, 9218 (2015).

[70] A. T. Hanbicki, M. Currie, G. Kioseoglou, A. L. Friedman, and B. T. Jonker, Measurement of high exciton binding energy in the monolayer transition-metal dichalcogenides WS_2 and WSe_2, Solid State Commun. **203**, 16 (2015).

[71] B. Han, C. Robert, E. Courtade, M. Manca, S. Shree, T. Amand, P. Renucci, T. Taniguchi, K. Watanabe, X. Marie, L. E. Golub, M. M. Glazov, and B. Urbaszek, Exciton states in monolayer $MoSe_2$ and $MoTe_2$ probed by upconversion spectroscopy, Phys. Rev. X **8**, 031073 (2018).

[72] C. Ferrara, E. Vigo, B. Albini, P. Galinetto, C. Milanese, C. Tealdi, E. Quartarone, S. Passerini, and P. Mustarelli, Efficiency and quality issues in the production of black phosphorus by mechanochemical synthesis: A multi-technique approach, ACS Appl. Energy Mater. **2**, 2794 (2019).

[73] X. Li, J. Sun, P. Shahi, M. Gao, A. H. MacDonald, Y. Uwatoko, T. Xiang, J. B. Goodenough, J. Cheng, and J. Zhou, Pressure-induced phase transitions and superconductivity in a black phosphorus single crystal, Proc. Natl. Acad. Sci. USA **115**, 9935 (2018).

[74] J. Cheng, L. Gao, T. Li, S. Mei, C. Wang, B. Wen, W. Huang, C. Li, G. Zheng, H. Wang, and H. Zhang, Two-dimensional black phosphorus nanomaterials: Emerging advances in

electrochemical energy storage science, Nanomicro Lett. **12**, 179 (2020).

[75] X. Ling, H. Wang, S. Huang, F. Xia, and M. S. Dresselhaus, The renaissance of black phosphorus, Proc. Natl. Acad. Sci. USA **112**, 4523 (2015).

[76] Y. Xu, Z. Shi, X. Shi, K. Zhang, and H. Zhang, Recent progress in black phosphorus and black-phosphorus-analogue materials: Properties, synthesis and applications, Nanoscale **11**, 14491 (2019).

[77] V. Tran, R. Soklaski, Y. Liang, and L. Yang, Layer-controlled band gap and anisotropic excitons in few-layer black phosphorus, Phys. Rev. B **89**, 235319 (2014).

[78] J. P. Perdew, K. Burke, and M. Ernzerhof, Generalized gradient approximation made simple, Phys. Rev. Lett. **77**, 3865 (1996).

[79] T. Kotani and M. van Schilfgaarde, All-electron GW approximation with the mixed basis expansion based on the full-potential LMTO method, Solid State Commun. **121**, 461 (2002).

[80] M. van Schilfgaarde, T. Kotani, and S. V. Faleev, Adequacy of approximations in GW theory, Phys. Rev. B **74**, 245125 (2006).

[81] F. Fuchs, J. Furthmüller, F. Bechstedt, M. Shishkin, and G. Kresse, Quasiparticle band structure based on a generalized Kohn-Sham scheme, Phys. Rev. B **76**, 115109 (2007).

[82] J. Heyd, G. E. Scuseria, and M. Ernzerhof, Hybrid functionals based on a screened coulomb potential, J. Chem. Phys. **118**, 8207 (2003).

[83] J. Heyd, G. E. Scuseria, and M. Ernzerhof, Erratum: "Hybrid functionals based on a screened coulomb potential" [J. Chem. Phys. **118**, 8207 (2003)], J. Chem. Phys. **124**, 219906 (2006).

[84] J. Qiao, X. Kong, Z.-X. Hu, F. Yang, and W. Ji, High-mobility transport anisotropy and linear dichroism in few-layer black phosphorus, Nat. Commun. **5**, 4475 (2014).

[85] P. Rinke, A. Qteish, J. Neugebauer, C. Freysoldt, and M. Scheffler, Combining GW calculations with exact-exchange density-functional theory: An analysis of valence-band photoemission for compound semiconductors, New J. Phys. **7**, 126 (2005).

[86] W. Chen and A. Pasquarello, Band-edge positions in *GW*: Effects of starting point and self-consistency, Phys. Rev. B **90**, 165133 (2014).

[87] L. Leppert, T. Rangel, and J. B. Neaton, Towards predictive band gaps for halide perovskites: Lessons from one-shot and eigenvalue self-consistent *GW*, Phys. Rev. Mater. **3**, 103803 (2019).

[88] A. N. Rudenko, S. Yuan, and M. I. Katsnelson, Toward a realistic description of multilayer black phosphorus: From *GW* approximation to large-scale tight-binding simulations, Phys. Rev. B **92**, 085419 (2015).

[89] V. Wang, Y. Kawazoe, and W. T. Geng, Native point defects in few-layer phosphorene, Phys. Rev. B **91**, 045433 (2015).

[90] M. Dai, C. Gao, Q. Nie, Q.-J. Wang, Y.-F. Lin, J. Chu, and W. Li, Properties, synthesis, and device applications of 2D layered InSe, Adv. Mater. Technol. **7**, 2200321 (2022).

[91] Y. Guo and J. Robertson, Band structure, band offsets, substitutional doping, and Schottky barriers of bulk and monolayer InSe, Phys. Rev. Mater. **1**, 044004 (2017).

[92] J. F. Sánchez-Royo, G. Muñoz-Matutano, M. Brotons-Gisbert, J. P. Martínez-Pastor, A. Segura, A. Cantarero, R. Mata, J.

Canet-Ferrer, G. Tobias, E. Canadell, J. Marqués-Hueso, and B. D. Gerardot, Electronic structure, optical properties, and lattice dynamics in atomically thin indium selenide flakes, Nano Res. **7**, 1556 (2014).

[93] S. Lei, L. Ge, S. Najmaei, A. George, R. Kappera, J. Lou, M. Chhowalla, H. Yamaguchi, G. Gupta, R. Vajtai, A. D. Mohite, and P. M. Ajayan, Evolution of the electronic band structure and efficient photo-detection in atomic layers of InSe, ACS Nano **8**, 1263 (2014).

[94] A. Politano, D. Campi, M. Cattelan, I. Ben Amara, S. Jaziri, A. Mazzotti, A. Barinov, B. Gürbulak, S. Duman, S. Agnoli, L. S. Caputi, G. Granozzi, and A. Cupolillo, Indium selenide: An insight into electronic band structure and surface excitations, Sci. Rep. **7**, 3445 (2017).

[95] D. A. Bandurin, A. V. Tyurnina, G. L. Yu, A. Mishchenko, V. Zólyomi, S. V. Morozov, R. K. Kumar, R. V. Gorbachev, Z. R. Kudrynskyi, S. Pezzini, Z. D. Kovalyuk, U. Zeitler, K. S. Novoselov, A. Patanè, L. Eaves, I. V. Grigorieva, V. I. Fal'ko, A. K. Geim, and Y. Cao, High electron mobility, quantum Hall effect and anomalous optical response in atomically thin InSe, Nat. Nanotechnol. **12**, 223 (2017).

[96] W. Gao, Z. Zheng, Y. Li, C. Xia, J. Du, Y. Zhao, and J. Li, Out of plane stacking of InSe-based heterostructures towards high performance electronic and optoelectronic devices using a graphene electrode, J. Mater. Chem. C **6**, 12509 (2018).

[97] J. Jiang, J. Li, Y. Li, J. Duan, L. Li, Y. Tian, Z. Zong, H. Zheng, X. Feng, Q. Li, H. Liu, Y. Zhang, T.-L. Ren, and L. Han, Stable InSe transistors with high-field effect mobility for reliable nerve signal sensing, npj 2D Mater. Appl. **3**, 29 (2019).

[98] H. Zheng, Y. Lu, K.-H. Ye, J. Hu, S. Liu, J. Yan, Y. Ye, Y. Guo, Z. Lin, J. Cheng, and Y. Cao, Atomically thin photoanode of InSe/graphene heterostructure, Nat. Commun. **12**, 91 (2021).

[99] M. Brotons-Gisbert, R. Proux, R. Picard, D. Andres-Penares, A. Branny, A. Molina-Sánchez, J. F. Sánchez-Royo, and B. D. Gerardot, Out-of-plane orientation of luminescent excitons in two-dimensional indium selenide, Nat. Commun. **10**, 3913 (2019).

[100] I. Paradisanos, S. Shree, A. George, N. Leisgang, C. Robert, K. Watanabe, T. Taniguchi, R. J. Warburton, A. Turchanin, X. Marie, I. C. Gerber, and B. Urbaszek, Controlling interlayer excitons in MoS$_2$ layers grown by chemical vapor deposition, Nat. Commun. **11**, 2391 (2020).

[101] N. Rytova, The screened potential of a point charge in a thin film, Mosc. Univ. Phys. Bull. **3**, 30 (1967).

[102] L. V. Keldysh, Coulomb interaction in thin semiconductor and semimetal films, JETP **29**, 658 (1979).

[103] M. L. Trolle, T. G. Pedersen, and V. Véniard, Model dielectric function for 2D semiconductors including substrate screening, Sci. Rep. **7**, 39844 (2017).

[104] S. T. Brown, P. Buitrago, E. Hanna, S. Sanielevici, R. Scibek, and N. A. Nystrom, Bridges-2: A platform for rapidly-evolving and data intensive research, in *Practice and Experience in Advanced Research Computing*, PEARC '21 (Association for Computing Machinery, New York, 2021).

[105] J. Towns, T. Cockerill, M. Dahan, I. Foster, K. Gaither, A. Grimshaw, V. Hazlewood, S. Lathrop, D. Lifka, G. D. Peterson, R. Roskies, J. R. Scott, and N. Wilkins-Diehr, Xsede: Accelerating scientific discovery, Comput. Sci. Eng. **16**, 62 (2014).

[106] G. Kresse and J. Furthmüller, Efficiency of *ab-initio* total energy calculations for metals and semiconductors using a plane-wave basis set, Comput. Mater. Sci. **6**, 15 (1996).

[107] G. Kresse and J. Furthmüller, Efficient iterative schemes for ab initio total-energy calculations using a plane-wave basis set, Phys. Rev. B **54**, 11169 (1996).

[108] P. E. Blöchl, Projector augmented-wave method, Phys. Rev. B **50**, 17953 (1994).

[109] G. Kresse and D. Joubert, From ultrasoft pseudopotentials to the projector augmented-wave method, Phys. Rev. B **59**, 1758 (1999).

[110] D. M. Ceperley and B. J. Alder, Ground state of the electron gas by a stochastic method, Phys. Rev. Lett. **45**, 566 (1980).

[111] J. P. Perdew and A. Zunger, Self-interaction correction to density-functional approximations for many-electron systems, Phys. Rev. B **23**, 5048 (1981).

[112] R. M. Martin, L. Reining, and D. M. Ceperley, *Interacting Electrons: Theory and Computational Approaches* (Cambridge University Press, Cambridge, UK, 2016).

[113] A. A. Mostofi, J. R. Yates, Y.-S. Lee, I. Souza, D. Vanderbilt, and N. Marzari, Wannier90: A tool for obtaining maximally-localised Wannier functions, Comput. Phys. Commun. **178**, 685 (2008).

[114] A. Tkatchenko and M. Scheffler, Accurate molecular Van Der Waals interactions from ground-state electron density and free-atom reference data, Phys. Rev. Lett. **102**, 073005 (2009).

[115] W. Schutte, J. De Boer, and F. Jellinek, Crystal structures of tungsten disulfide and diselenide, J. Solid State Chem. **70**, 207 (1987).

[116] L. M. Kulikov, A. A. Semenov-Kobzar', L. G. Aksel'rud, T. A. Lobova, and E. A. Bogachev, Niobium, molybdenum and tungstem diselenide intercalation by copper, zinc, gallium, Neorg. Mater. **28**, 525 (1992).

[117] L. Cartz, S. R. Srinivasa, R. J. Riedner, J. D. Jorgensen, and T. G. Worlton, Effect of pressure on bonding in black phosphorus, J. Chem. Phys. **71**, 1718 (1979).

[118] K. El-Sayed, Z. K. Heiba, K. Sedeek, and H. H. Hantour, Magnetic, electric and crystallographic properties of diluted magnetic $InSe_{(1-x)}Fe(Co)_x$ semiconductor, J. Alloys Compd. **530**, 102 (2012).

[119] B. Schönfeld, J. J. Huang, and S. C. Moss, Anisotropic mean-square displacements (MSD) in single-crystals of 2H- and $3R-MoS_2$, Acta. Crystallogr. B Struct. Sci. **39**, 404 (1983).

[120] A. Brager, An x-ray examination of the structure of boron nitride, Acta Physicochim. (USSR) **7**, 699 (1937).

[121] H. Jiang, Electronic band structures of molybdenum and tungsten dichalcogenides by the GW approach, J. Phys. Chem. C **116**, 7664 (2012).

[122] M. Graml, K. Zollner, D. Hernangómez-Pérez, P. E. Faria Junior, and J. Wilhelm, Low-scaling GW algorithm applied to twisted transition-metal dichalcogenide heterobilayers, arXiv:2306.16066.

[123] S. Haastrup, M. Strange, M. Pandey, T. Deilmann, P. S. Schmidt, N. F. Hinsche, M. N. Gjerding, D. Torelli, P. M. Larsen, A. C. Riis-Jensen, J. Gath, K. W. Jacobsen, J. J. Mortensen, T. Olsen, and K. S. Thygesen, The computational 2D materials database: high-throughput modeling and discovery of atomically thin crystals, 2D Mater. **5**, 042002 (2018).

[124] M. N. Gjerding, A. Taghizadeh, A. Rasmussen, S. Ali, F. Bertoldo, T. Deilmann, N. R. Knøsgaard, M. Kruse, A. H. Larsen, S. Manti, T. G. Pedersen, U. Petralanda, T. Skovhus, M. K. Svendsen, J. J. Mortensen, T. Olsen, and K. S. Thygesen, Recent progress of the computational 2D materials database (C2DB), 2D Mater. **8**, 044002 (2021).

[125] H.-P. Komsa and A. V. Krasheninnikov, Effects of confinement and environment on the electronic structure and exciton binding energy of MoS_2 from first principles, Phys. Rev. B **86**, 241201(R) (2012).

[126] F. Paleari, T. Thomas Galvani, H. Amara, F. Ducastelle, A. Molina-Sánchez, and L. Wirtz, Excitons in few-layer hexagonal boron nitride: Davydov splitting and surface localization, 2D Mater. **5**, 045017 (2018).